Polarimetric weather signatures and Doppler spectral analysis of a convective squall line

Ricardo Reinoso-Rondinel[1], Christine Unal[1], Herman Russchenberg[1], Thijs IJpelaar[1], and Yann Dufournet[1]

[1]*Department of Geoscience and Remote Sensing, Delft University of Technology, 2628CN Delft, Netherlands*

(Dated: 9 September 2014)

1. Introduction

Continuous upgrades on conventional weather radars have benefited research and operational weather communities. In Europe, the Operational Program for the Exchange of weather RAdar information (OPERA) is currently the network of weather radars (Huuskonen et al., 2012). OPERA consists mainly of 194 single-polarimetric S- and C-bands radars with temporal and spatial resolutions of approximately 5 min and 1 km, respectively. The Netherlands (NL) have contributed to OPERA with two C-bands radars operated by the Royal Netherlands Meteorological Institute (KNMI in Dutch initials and hereafter KNMI radars). As a result, observations of multiple hazardous weather events have been reported and studied. For example, Groenemeijer (2005) has identified and described storm types associated with lightning activities, severe wind gusts, and large hail damages. Efforts in obtaining accurate radar rain rate (R) of flash flooding storms have been shown by Hazenberg et al. (2014). Although such achievements obtained using conventional radars, their temporal and spatial resolutions might not be sufficient to detect small but threatening features of fast-evolving convective weather (Carbone et al., 1985; Steadham et al., 2002). For example, Clark (2011); Grumm and Glazewski (2004); Lane and Moore (2006); McAvoy et al. (2000) have shown that early tornadoes signatures associated with non-supercell storms are difficult to detect using conventional radar. Thus, early warning of possible non-supercell tornadic storms (NSTs) remains a considerable challenge to forecasters (Baumgardt et al., 2006; Davis and Parker, 2014; Smith, 1996). Nevertheless, one way to obtain fast and close observations of severe storms is using X-band radars with resolutions higher than these of conventional radars. For example, the research Center for Collaborative Adaptive Sensing of the Atmosphere (CASA) consists of a network of dual-polarimetric X-band radars with temporal and spatial resolutions of approximately 1 min and 100 m, respectively (McLaughlin et al., 2009). In Western Europe, the RainGain project is working in the implementation of X-band radars to capture the spatial and temporal variability of heavy rainfall events in urbanized cities (http://www.raingain.eu).

In this work, the dual-polarimetric X-band (IDRA) and S-band vertical profiler (TARA) weather radars, located in the Cabauw Experimental Site for Atmospheric Research (CESAR) observatory of the NL, were used to obtain detailed observations of a cold-season organized storm. On January 03 2012, a squall line storm moving over Western Europe was observed using the KNMI, IDRA, and TARA radars. Moreover, the numerical prediction model HIRLAM ALADIN Research on Mesoscale Operational NWP In Euromed (HARMONIE) was used to simulate the evolution of the squall line event. It will be shown that the squall line progressively broke into multiple bowed-shaped segments associated with the S-broken reflectivity pattern; and rear and forward inflow notches (Davis and Parker, 2014; McAvoy et al., 2000). Davis and Parker (2014); Nolen (1959) have associated these signatures with non-tornadic and tornadic non-supercell vortices, mostly squall lines vortices. However, detailed observations using IDRA and TARA revealed reflectivity signatures such as hook echo and weak echo region (WER) which are associated with supercell vortices. Moreover, Doppler moments profiles and spectograms using TARA will show the updraft and downdraft circulation and small-scale turbulence. This paper is organized as follows. In section 2, the weather environment will be described using satellite observations and sounding measurements. Description of the squall line, moving over the NL, will be presented in section 3 using operational weather radars and numerical modeling. In section 4, detailed horizontal and vertical observations will be introduced using IDRA and TARA to explain storm dynamic processes related to Doppler moments, polarimetric signatures, and spectograms. Finally, conclusions are given in section 5.

2. Environment description

As mentioned previously, early detection of tornadic and non-tornadic vortices associated with non-supercell storms remain a challenge for forecasters. It has been reported that most of these vortices were observed within quasi-linear convective systems (QLCS) associated with strong synoptic force, convective available potential energy (CAPE) smaller than 500 J Kg^{-1}, and low-level wind shear larger than 20 m s^{-1}. The environment condition where the squall line developed is introduced next using satellite observations and sounding measurements.

Thermal infrared (IR) satellites are used to measure cloud temperatures and in consequence cold and warm fronts could be distinguished (Ahrens, 2012). Cold fronts lift warm moist air and produce cold and vertical developing clouds. In this work, a cold front over the North Sea in Europe was observed by the IR satellite SAT24-EISQ51 on January 03 2012 as shown in Figure 1. Panel a) shows a cold (white) cyclonic system at 12:00 UTC located on the North Sea and moving

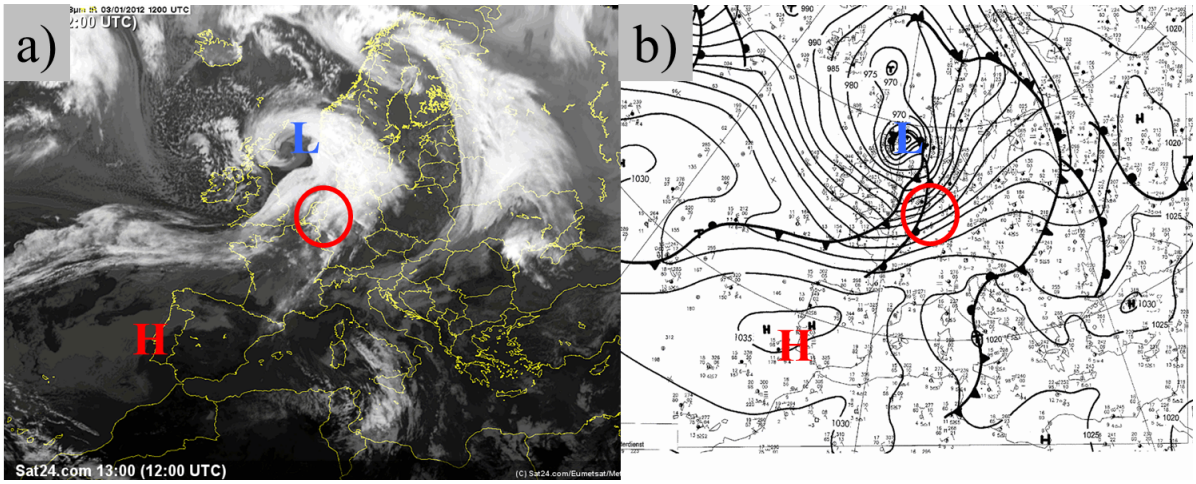

Figure 1: Panel a) shows an infrared (IR) satellite imagery from SAT24-EISQ51 over Europe on 12:00 UTC, 03 January 2012 showing the strong frontal zone over the Netherlands associated with a deep low pressure system centered over the North Sea. Panel b) displays the corresponding synoptic chart at ground level, courtesy of the German Weather Service.

eastward. The pressure surface analysis map at 12:00 UTC is shown in panel b). The low pressure of 953 hPa, denoted by the blue letter L, is in the center of the cyclone where a warm front is followed by a cold front led by the low and high pressure systems. The red circle denotes the location of the NL where a radiosonde in De Bilt station was launched at 12:00 UTC (http://weather.uwyo.edu/upperair/sounding.html). Wind measurements showed a clear profile for the development of organized convection with wind shear of 26 m s^{-1} between 0 and 5 km (non shown). In contrast to previous reported instability values associated with cool-season squall lines, the environment, at 12:00 UTC, was very stable resulting in negligible CAPE. Therefore, this case study will be referred as a shallow cool-season convective system associated mainly with strong synoptic force and wind shear, as shown by the IR satellite and sounding measurements, respectively. The next section will be focused on weather observation and simulation of the shallow QLCS over the Netherlands.

3. Operational radar observations and numerical simulation

One of the most fundamentals weather radar products is the so-called reflectivity (Z). Reflectivity is related to signal power and depends on the number of hydrometeors per unit volume, size, physical state, and shape of hydrometeors (Doviak and Zrnić, 1993). In this section, observations using the KNMI operational radars (Beekhuis and Holleman, 2008) will be shown. In addition the high resolution numerical model HARMONIE will be used to simulate the line evolution (Krikken, 2012).

Each of the KNMI radars has a maximum range of 320 km with a range resolution of 1.0 km approximately. Ground clutter was removed and composited reflectivity at constant height of 1.5 km was obtained by interpolating reflectivity pixels from both radars at elevations angles of 0.3, 1.1, 2.0, and 3.0^0 (Beekhuis and Holleman, 2008). The reflectivity field at 14:40 UTC is shown in Figure 2 a). The red circle denotes approximately the 320 km range coverage centered between both KNMI radars. It can be seen that the squall line has been broken into several bowing segments, with $Z > 30$ dBZ, indicated by the black arrows.

HARMONIE is a research weather model focused on forecasting convective weather scenarios. In our setup, its horizontal domain extends up to 750 km with a 2.5 km grid resolution and 60 vertical layers. Among other parameters, rainfall rate was simulated at 10 m from ground level for a period of six hours, every 10 min, starting at 12:00 UTC . Since the estimation of rainfall rate is not the scope of this work, the Marshall-Palmer relationship given by $Z = 200.R^{1.6}$ was used to simulate reflectivity. Deceleration of the storm motion was observed while the simulated convective line was approaching the coast of the NL. For example, at 14:40 UTC, the simulated reflectivity field showed a temporal delay of 1 hr and 15 min, approximately, as shown in Figure 2 b). The 30 dBZ reflectivity segments from KNMI observations are plotted on top and denoted by red contours. Although the simulated squall line moved slower than the actual observed, its reflectivity field showed similar pattern of several broken segments.

S-broken signatures have been associated with tornadic and non-tornadic non-supercell storms, mainly shallow QLCS (McAvoy et al., 2000). In general, the S-broken signature consists of two bowing segments that result of the break of a convective line where the southern segment moves ahead of the northern segment forming an S-shaped broken signature. In fact, Clark (2011); Grumm and Glazewski (2004); Lane and Moore (2006); McAvoy et al. (2000) have argued that the fragmentation of a shallow line might result from a rear inflow jet (RIJ) force. An example of the S-broken reflectivity is given in Figure 3 which is similar to Figure 2 but only over the NL and centered at 5.5^oE and 52^oN. The S-broken reflectivity signature is indicated by curved black lines in panels a) and b) for KNMI radars and Harmonie model, respectively. Moreover, it has been reported that tornado and non-tornado vortex associated with S-broken signatures typically occurs near the south-end

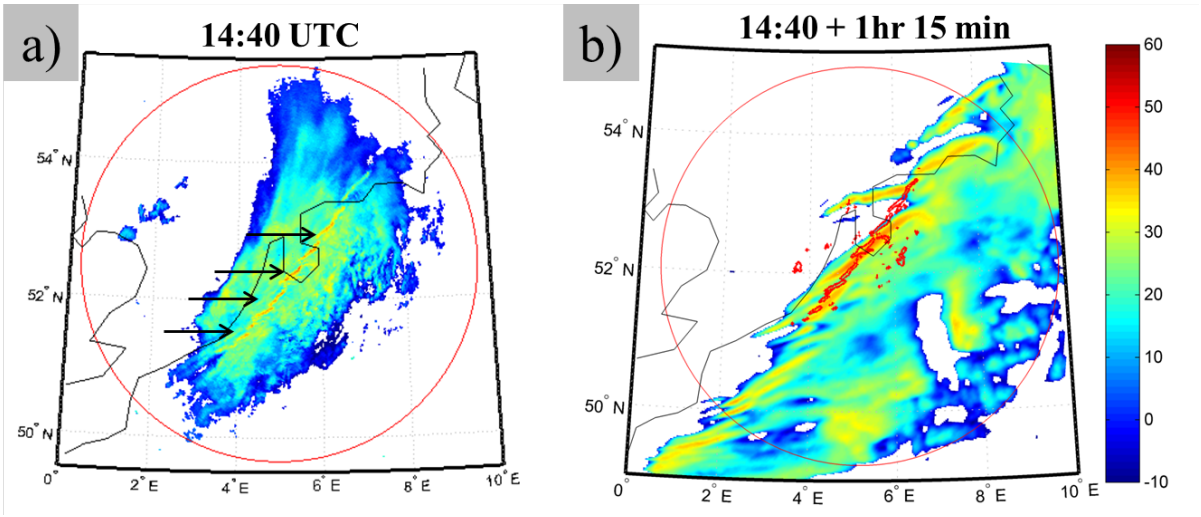

Figure 2: Panel a) shows the reflectivity field associated with a line echo wave pattern (LEWP) at 14:40 UTC and obtained from the KNMI radars. Panel b) displays the derived reflectivity from the simulated QPE using HARMONIE. Note that there is a time delay between the observed and simulated QLCS of 1 hr and 15 min approximately.

of the northern segment but their dynamics process remain mostly unexplored (Davis and Parker 2014). Therefore two research radars, controlled by the Delft University of Technology, located in the center of the red circle shown in Figure 3 a) are introduced in the next section for high resolution observations.

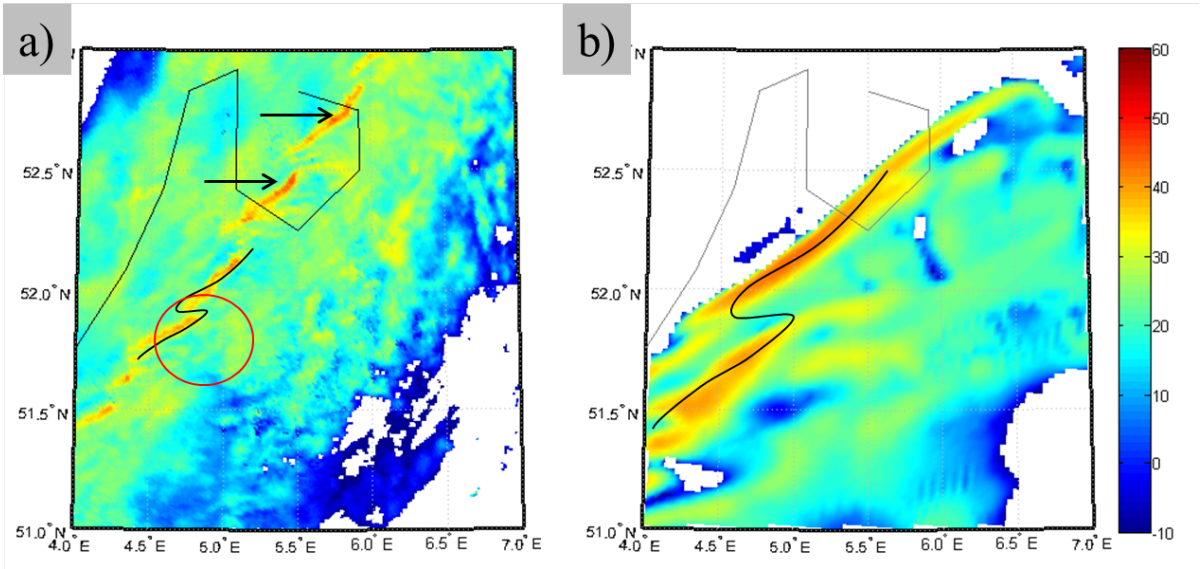

Figure 3: Similar to Figure 2 but showing the S-broken signature. In addition, bowing segments are indicated by black arrows.

4. Research weather radar observations

4.1. Horizontal-scan observations: polarimetric X-band radar (IDRA)

IDRA is one of the research radars installed in CESAR observatory (Figueras i Ventura, 2009). The standard operational range is of 15 km with spatial resolution of 30 m. It scans at a fixed elevation angle of 0.5^0 and rotates the antenna over 360^0 every 1 min. Reflectivity samples obtained by KNMI and IDRA radars are shown in Figure 4. Top row shows KNMI reflectivity snapshots from 14:40 to 14:50 UTC sampled every 5 min and limited to IDRA range extent of 15 km. The northern and southern segments associated with the S-broken signature are shown at 14:40 UTC. At 14:45 UTC, the south-end of the northern segment shows a hook appendage. This might indicate that the rear inflow jet has turned cyclonic (Lane and Moore, 2006). Five minutes after, 14:50 UTC, the appendage signature vanished while both segments kept moving eastward.

For QLCS vortices, radar signatures include mainly the rear inflow notch (RIN), bowing segments, and the forward inflow notch (FIN) (Przybylinski, 1995; Trapp and Weisman, 2003). In addition, Thompson et al. (2012) have shown that shallow QLCS vortices might lead to the development of weak tornadoes. Bottom row shows six reflectivity snapshots between 14:37 and 14:47 UTC showing the evolution of the S-broken signature measured by IDRA. At 14:37 UTC, the northern and southern

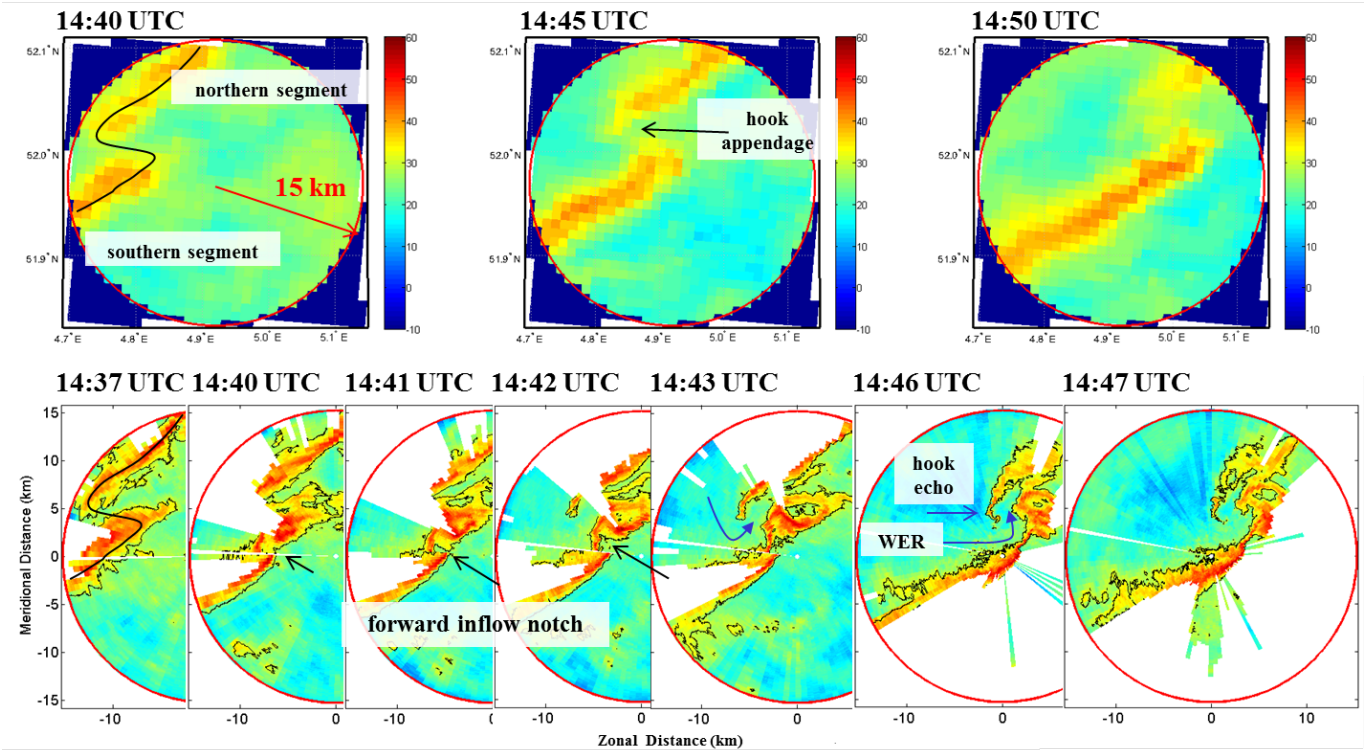

Figure 4: Top panels show the reflectivity field using KNMI radars over IDRA coverage. Bottom panels shows the reflectivity field using IDRA showing the S-reflectivity signature, hook-echoes, and weak echoes regions (WERs).

segments are indicated by the 30 dBZ contour level. Three minutes after, 14:40 UTC, a small indentation in the southern segment is indicated by the black arrow. Such indentation is more evident during 14:41 and 14:42 UTC producing the so-called forward inflow notch signature and might indicate the presence of strong warm moist inflow. The northern segment shows a narrow appendage, at 14:43 UTC, surrounded by low reflectivity values of 20 dBZ approximately. Three minutes after, 14:46 UTC, the appendage is more pronounced showing the hook echo and the weak echo region which are reflectivity signatures associated with supercell storms and might indicate the presence of vorticity and strong updraft (Lemon and Doswell, 1979). Although the hook echo is still visible at 14:47 UTC, the south-end of the northern segment storm started to dissipate while the north-end of the southern segment shows a visible rear inflow notch that pushes and curves its rear side. Due to currently IDRA limitations of the maximum unambiguity Doppler radial velocity of 18 m s^{-1} and lack of tornado damage report, it is still unknown to the authors whether or not these vortices, associated with the S-broken signature, produced any tornado. The white areas mean that signals were strongly corrupted by attenuation and therefore no reflectivity estimates were shown. For a first insight of polarimetric signatures, the observations using the specific differential phase are introduced next.

Polarimetric variables have been used to identify weather signatures of tornadic and non-tornadic supercells (Bluestein et al., 2006; Crowe et al., 2012; Schwarz and Burgess, 2011; Snyder et al., 2013). In this work the specific differential phase will be discussed. The specific differential phase (K_{dp}) increases for large oblate-shaped drops and for a large number of particles within a resolution volume. As a result, one of the primary advantages of K_{dp} is to identify areas of heavy rainfall. Typical values of K_{dp} at X-band are between 0 and 7 deg km^{-1} but very heavy rainfall can produce larger K_{dp} values (Snyder et al., 2010). In this work, K_{dp} was estimated based on the technique introduced by Otto and Russchenberg (2011), where the differential backscatter phase is estimated and then removed from the accumulated differential phase difference. As a positive result the estimated K_{dp} will not account for the non-Rayleigh scattering effect that occurs at X-band wavelengths. K_{dp} estimates related to the S-broken IDRA reflectivity signature are shown in Figure 5. At 14:37 UTC, the southern segment included K_{dp} values between 2 and 3 deg km^{-1} but at 14:40 and 14:41 UTC, K_{dp} increased to 7 deg km^{-1} approximately. However, neither reflectivity (shown) nor differential reflectivity (not shown) values presented significant increase during these sampled times. Such increase in K_{dp} might result from a large concentration of probably small drops that are advected by the inflow air associated with the forward inflow notch, shown in Figure 4. Similar process in QLCS have been shown by Crowe et al. (2012). At 14:42 UTC, lines of highly concentrated drops are still noticeable and at 14:43 UTC, these drops are shifted further back from the edge inflow resulting in pronounced curved-line along with large K_{dp} values. Non-significant physical interpretation can be derived using K_{dp} from the northern segment mainly because large areas were removed due to low signal to noise ratio (attenuation problem). Vertical profiles associated with the southern segment and measured by the profiler radar TARA are depicted next.

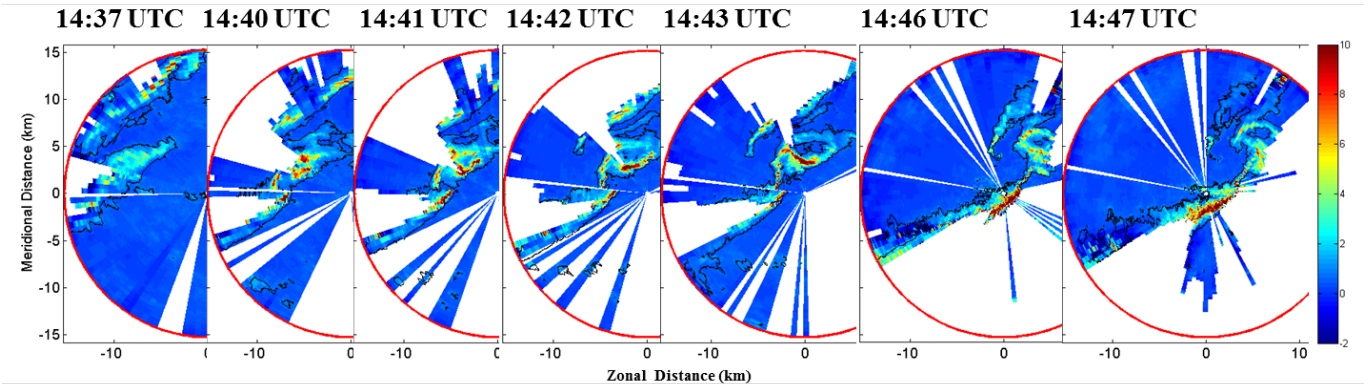

Figure 5: Similar to Figure 4 but for the specific differential phase in deg km $^{-1}$ units. Note that the southern segment showed enhanced K_{dp} values while the forward inflow notch signature persists.

4.2. Vertical observations: profiler S-band radar (TARA)

The research profiler radar TARA has dual-polarimetric capabilities and works at S-band (3.3 GHz), (Heijnen et al., 2000; Unal et al., 2012). The elevation angle can be set manually between 0^0 (horizontal) and 90^0 (vertical). Profiles can be sampled every 2.5 sec with a range coverage of 15 km and range resolution of 30 m. Signal processing algorithms, implemented in TARA, to improve ground clutter removal, Doppler dealiasing, and wind retrieval can be found in Ibánez (2008); Unal (2009); Unal and Moisseev (2004).

In this work, the elevation angle of TARA, located 339 m aways from IDRA, was set to 90^0. The Doppler moments: reflectivity, mean Doppler velocity, and spectrum width are shown in Figure 6. The x-axis express the time from 14:35 to 14:55 UTC, approximately, and the y-axis the height in meters. The top panel shows the height-time reflectivity profiles which intercept the southern segment of the S-broken pattern shown in Figure 4. The bright-band is indicated by the dashed ellipsoid and is located around 1700 m which is consistent for cold season storms. It can be seen that the convective segment extends vertically only to 3500 m approximately. Around 14:45 UTC, the reflectivity profiles showed similar features of these of the supercell conceptual model, such as the reflectivity overhang, given by Lemon and Doswell (1979), but at smaller scales. The black contour line indicates a 35 dBZ level associated with the reflectivity overhang and bounded weak echo region (BWER). The updraft-downdraft circulation can be seen in the middle panel, the vertical mean Doppler velocity. The updraft reaches values larger than 5 m s^{-1} and it is surrounded by two downdraft regions with falling velocities larger than 5 m s $^{-1}$. Aliased velocities profiles are shown by the red lines and after 14:46 UTC approximately. The lower panel shows the Doppler spectrum width which is related to drop size distribution and wind shear (Kollias et al., 2001). At 14:45 UTC approximately, large spectrum widths might result from falling and rising drops that were observed within the same resolution volume. During the next 5 min between 1500 and 3000 m, large values of spectrum width can be found as a consequence of the mixing of two air masses, the warm moist air that is lifted by the cold front and merged with air back of the storm. Spectograms were also measured. They are introduced next.

Weather spectograms are used to examine the power distribution in Doppler domain (Doviak and Zrnić, 1993). In this work, Range-Doppler spectograms, hereafter spectograms, were obtained using TARA for each vertical profile to show small- scales dynamic processes of the convective line along the boresight of TARA. Spectograms in dBZ units for six temporal instants are shown in Figure 7. At 14:43:02 UTC, the spectogram showed stratiform-like echoes but very low echoes within the lowest 500 m and falling at 5 m s^{-1} approximately. At 14:44:01 UTC, an increased in reflectivity can be seen but with falling velocities smaller than 5 m s^{-1}. At 14:44:33 UTC, the spectogram column, up to 2000 m, was shifted to the right-hand side of the Doppler domain, positive Doppler. This means that particles are now rising by a strong updraft. Above 2000 m, spectograms with strong reflectivity, wide, and centered at 0 m s^{-1} might result from the updraft-downdraft circulation within the same resolution volume. Lifted raindrops freeze and increase the sizes of ice aggregates (heavy aggregation process). The reflectivity is larger and the fall velocity compensates the updraft velocity. At 14:44:59 UTC the spectogram column shows a discontinuity in range, which might be due by the convergence boundaries between the lifted warm moist air and the cold front. Above 2000 m, spectograms show particles led by a localized downdraft-updraft circulation. Below it, rapidly descendant particles, that is dominated by downdraft circulation, reach the surface with terminal velocities of 10 m s^{-1} approximately. At 14:45:26 UTC, wide and enhanced spectograms reaching the ground with falling velocities around 8 m s^{-1} indicate a downdraft circulation associated with heavy precipitation resulting from melting of the large aggregates. Finally, at 14:46:30 UTC, spectograms still show precipitation around 8 m s^{-1} but with weaker reflectivity and smaller spectrum width values.

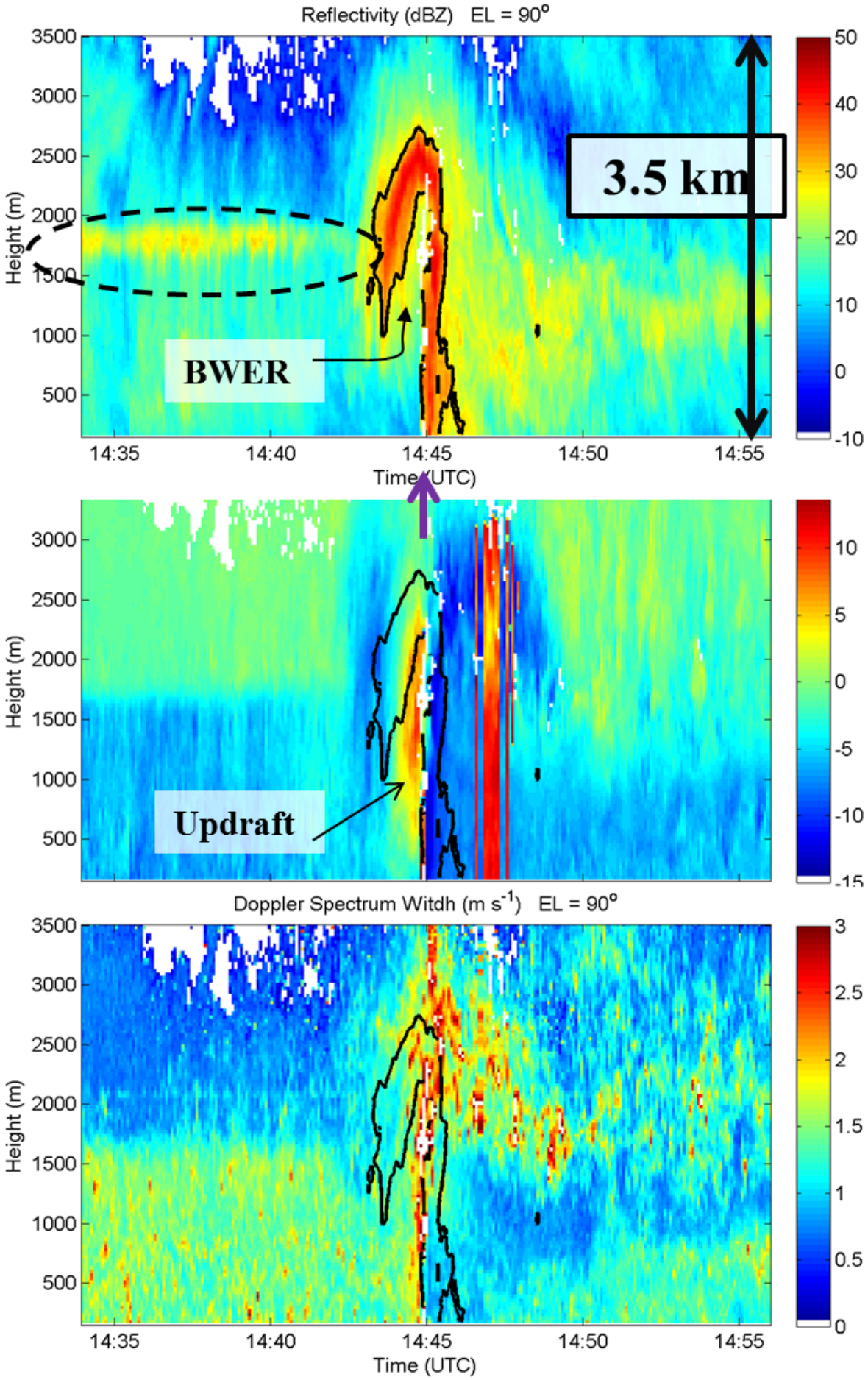

Figure 6: Doppler moments. Top panel: the reflectivity shows similar signatures to these of tornadic supercells storms. Center panel: the mean Doppler velocity in panel b) exhibits an updraft surrounded by two downdraft regions. Turbulent and convergent areas can be observed from the Doppler spectrum width, bottom panel.

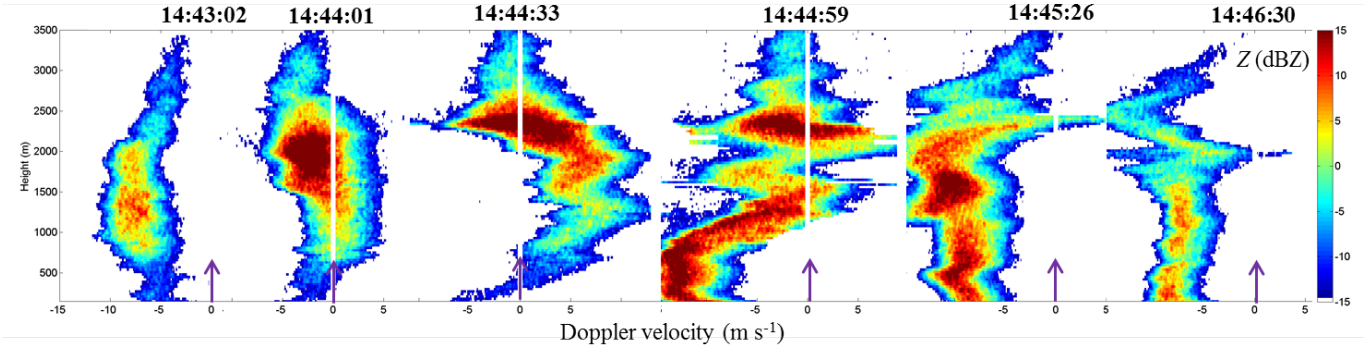

Figure 7: Range-Doppler spectograms obtained by TARA and sampled during the updraft-downdraft circulation. Note that gap between fast falling and suspended particles at 14:44:59 UTC.

5. Conclusions

Conventional weather radars usually coverage a large spatial domain but limited to obtain observations of small features at low spatial and temporal resolutions. X-band radars are suitable to obtain detail observations and possibly overcome such limitation. Small scales features related to a shallow but high low-level wind shear convective squall line were observed to identify rotation patterns.

A quasi-linear convective system (QLCS) was used to test the capability of high resolution systems such as a numerical model, X-band radar, and S-band radar denominated as HARMONIE, IDRA, and TARA, respectively, for the detection and interpretation of small rotation signatures. HARMONIE was able to simulate the evolution, structure, and reflectivity values of the QLCS as compared with observations by the operational KNMI weather radars. However, the motion of the simulated QLCS was not as fast as the one observed by the KNMI radars and therefore model parameters linked with the storm motion might need further research. In the reflectivity field, it was possible to identify the so-called S-broken pattern from radar observations and numerical simulations. However, high resolutions observations obtained by IDRA were able to capture signatures such as the rear (front) inflow notches, hook echo, and the weak echo regions typically associated with tornadic and non-tornadic vortices. Moreover, vertical profiles obtained by TARA showed a strong updraft-downdraft circulation and a bounded weak echo region which are not usually associated with QLCS but with mature tornadic supercells.

In summary, high resolution weather observation are important for obtaining small but threatening storm futures. As illustrated in this work, such X-band dual polarimetric IDRA should be used to obtain detailed and fast weather observations. It is foreseen that the identification of the environment conditions and high resolutions weather observations and modeling would improve the understanding, detection and therefore warning lead times associated with tornadic non-supercell storms such QLCS.

Acknowledgment

This work was supported by INTERREG IVB North-West Europe (NWE) project RainGain. The authors acknowledge KNMI for providing weather radar data.

References

C. D. Ahrens, *Meteorology Today: An Introduction to Weather, Climate, and the Environment*, 10th ed. Belmont, CA, USA: Cengage Learning, 2012.

D. A. Baumgardt, L. Crosse, and K. Cook, "Preliminary evaluation of a parameter to forecast environments conducive to non-mesocyclone tornadogenesis," in 23^{rd} *Conference on severe local storms*, 2006.

H. Beekhuis and I. Holleman, "From pulse to product: Highlights of the digital-IF upgrade of the Dutch national radar network," in 5^{th} *European Conference of Radar Meteorology and Hydrology*, Helsinki, Finland, April 2008.

H. Bluestein, M. French, R. Tanamachi, S. Frasier, K. Hardwick, F. Junyent, and A. Pazmany, "Close-range observations of tornadoes in supercells made with a dual-polarization, X-band, mobile Doppler radar," *Mon. Wea. Rev.*, vol. 135, pp. 1522–1543, 2006.

R. E. Carbone, M. J. Carpenter, and C. D. Burghart, "Doppler radar sampling limitations in convective storms," *J. Atmos. Oceanic Technol.*, vol. 2, pp. 357–361, 1985.

M. Clark, "Doppler radar observations of mesovortices within a cool-season tornadic squall line over the UK," *Atmos. Res.*, vol. 100, pp. 749–764, 2011.

C. Crowe, C. Schultsz, M. Kumjian, L. Carey, and W. Petersen, "Use of dual-polarization signatures in diagnosing tornadic potential," *Electronic J. Operational Meteor.*, vol. 13, pp. 57–78, 2012.

J. Davis and M. Parker, "Radar climatology of tornadic and nontornadic vortices in high-shear, low-CAPE environments in the mid-atlantic and southeastern United States," *Wea. Forecasting*, vol. 29, pp. 828–853, 2014.

R. J. Doviak and D. S. Zrnić, *Doppler Radar and Weather Observations*. San Diego, Calif.: Academic, 1993.

J. Figueras i Ventura, "Design of a high resolution X-band doppler polarimetric radar," Ph.D. dissertation, Delft University of Technology, 2009.

P. Groenemeijer, "Three events of strong deep moist convection in the Netherlands," KNMI, Tech. Rep., 2005.

R. H. Grumm and M. Glazewski, "Thunderstorm types associated with the "broken-S" radar signature," in 22^{nd} *Conf. on Severe Local Storms*. Hyannis, MA: Amer. Meteor. Soc., 2004.

P. Hazenberg, H. Leijnse, and R. Uijlenhoet, "The impact of reflectivity correction and conversion methods to improve precipitation estimation by weather radar for an extreme low-land mesoscale convective system," in *Int. Symp. - Wea. Radar and Hydro.* ASCE-EWRI, 2014.

S. Heijnen, L. Ligthart, and H. Russchenberg, "First measurement with TARA: An S-band transportable atmopsheric radar," *Phys. Chem. Earth*, vol. 25, pp. 995–998, 2000.

A. Huuskonen, L. Delobe, and B. Urban, "EUMETNET OPERA: Achievements of OPERA-3 and challenges ahead," in 7^{th} *European Conf. on Radar in Meteo. and Hydrol.*, 2012.

M. G. Ibánez, "Validation of wind retrieval algorithm for TARA using other wind sensors," Master's thesis, Delft University of Technology, 2008.

P. Kollias, B. Albrecht, R. Lhermitte, and A. Savtchenko, "Radar observation of updraft, downdrafts, and turbulence in fair-weather cumuli," *Journal of the Atmospheric Sciences*, vol. 58, pp. 1750–1766, July 2001.

F. Krikken, "Sensitivity analysis for a model physics in HARMONIE," KNMI, Trainee Report, 2012. [Online]. Available: http://www.knmi.nl/knmi-library/traineereport.html

J. D. Lane and P. D. Moore, "Observations of a non-supercell tornadic thunderstorm from a terminal Doppler weather radar," in 23^{rd} *Conf. on Severe Local Storms*. St. Louis, AB: Amer. Meteor. Soc., 2006.

L. R. Lemon and C. A. Doswell, "Severe thunderstorm evolution and mesocyclone structure as related to tornadogenesis," *Mon. Wea. Rev.*, vol. 107, pp. 1184–1197, 1979.

B. P. McAvoy, W. A. Jones, and P. D. Moore, "Investigation of an unusual storm structure associated with weak to occasionally strong tornadoes over the Eastern United States," in 20^{th} *Conf. on Severe Local Storms*. Orlando, FL,: Amer. Meteor. Soc., 2000.

D. McLaughlin, D. Pepyne, B. Philips, J. Kurose, M. Zink, D. Westbrook, E. Lyons, E. Knapp, A. Hopf, A. Defonzo, R. Contreras, T. Djaferis, E. Insanic, S. Frasier, V. Chandrasekar, F. Junyent, N. Bharadwaj, Y. Wang, Y. Liu, B. Dolan, K. Droegemeier, J. Brotzge, M. Xue, K. Kloesel, K. Brewster, F. Carr, S. Cruz-Pol, K. Hondl, and P. Kollias, "Short-wavelength technology and the potential for distributed networks of small radar systems," *Bull. Amer. Meteor. Soc.*, vol. 90, no. 12, pp. 1797 – 1817, 2009.

R. H. Nolen, "A radar pattern associated with tornadoes," *Bull. Amer. Meteor. Soc.*, vol. 40, pp. 277–279, 1959.

T. Otto and H. W. J. Russchenberg, "Estimation of specific differential phase and differential backscatter phase from polarimetric weather radar measurements of rain," *IEEE Geoscience and Remote Sensing Letters*, vol. 8, pp. 988–992, 2011.

R. Przybylinski, "The bow echo: Obeservations, numerical simulations, and severe weather detection methods," *Wea. Forecasting*, vol. 10, 1995.

C. Schwarz and D. Burgess, "Supercell polarimetric signatures at X-band: Data from VORTEX2," in *35th Conf. on Radar Meteor., AMS*, 2011.

R. Smith, "Non-supercell tornadoes: A review for forecasters," NWSFO Memphis, Technical Attachment, 1996. [Online]. Available: http://www.srh.noaa.gov/topics/attach/html/ssd96-8.htm

J. Snyder, H. Bluestein, and G. Zhang, "Attenuation correction and hydrometeor classification of high-resolution, X-band, dual-polarized mobile radar measurements in severe convective storms," *Journal of Atmospheric and Oceanic Technology*, vol. 27, pp. 1979–2001, 2010.

J. Snyder, H. Bluestein, V. Venkatesh, and S. Frasier, "Observations of polaimetric signatures in supercells by an x-band mobile Doppler radar," *Mon. Wea. Rev.*, vol. 141, pp. 3 – 29, 2013.

R. M. Steadham, R. A. Brown, and V. T. Wood, "Prospects for faster and denser WSR-88D scanning strategies," in *18th Int. Conf. on Interactive Information and Processing Systems (IIPS) for Meteorology, Oceanography, and Hydrology*. Orlando, FL, Amer. Meteor. Soc., J3.16, 2002.

R. L. Thompson, B. Smith, J. S. Grams, A. R. Dean, and C. Broyles, "Convective modes for significant severe thunderstorms in the contiguous United States. part II: Supercell and QLCS tornado environments," *Wea. Forecasting*, vol. 27, pp. 1136 – 1154, 2012.

R. Trapp and M. Weisman, "Low-level mesovortices within squall lines and bow echoes. Part II: Their genesis and implications," *Mon. Wea. Rev.*, vol. 131, pp. 2804–2823, 2003.

C. Unal, "Spectral polarimetric radar clutter suppression to enhance atmospheric echoes," *J. Atmos. Oceanic Technol.*, vol. 26, pp. 1781–1797, 2009.

C. Unal, Y. Dufournet, T. Otto, and H. Russchenberg, "The new real-time mesurement capabilities of the profiling TARA radar," in *ERAD 2012 - The 7th European Conference on Radar in Meteorology and Hydrology*, 2012.

C. M. H. Unal and D. N. Moisseev, “Combined Doppler and polarimetric radar measurements: Correction for spectrum aliasing and nonsimultaneous polarimetric measurements,” *J. Atmos. Oceanic Technol.*, vol. 21, pp. 443–456, 2004.